

# Three-Dimensional Giant Invisibility to Superscattering Enhancement Induced by Zeeman-Split Modes

Grigorios P. Zouros,<sup>\*,†,‡</sup> Georgios D. Kolezas,<sup>‡</sup> Evangelos Almpanis,<sup>†,¶</sup> and Kosmas  
L. Tsakmakidis<sup>\*,†</sup>

<sup>†</sup>*Section of Condensed Matter Physics, National and Kapodistrian University of Athens,  
Panepistimioupolis, GR-157 84 Athens, Greece*

<sup>‡</sup>*School of Electrical and Computer Engineering, National Technical University of Athens,  
Athens 15773, Greece*

<sup>¶</sup>*Institute of Nanoscience and Nanotechnology, NCSR “Demokritos”, Patriarchou  
Gregoriou and Neapoleos Street, Ag. Paraskevi, GR-153 10 Athens, Greece*

E-mail: zouros@mail.ntua.gr; ktsakmakidis@phys.uoa.gr

## Abstract

We report that the fundamental three-dimensional (3-D) scattering single-channel limit can be exceeded in magneto-optical assisted systems by inducing nondegenerate magnetoplasmonic modes. In addition, we propose a 3-D active (magnetically assisted) forward-superscattering to invisibility switch, functioning at the same operational wavelength. Our structure is composed of a high-index dielectric core coated by indium antimonide (InSb), a semiconductor whose permittivity tensorial elements may be actively manipulated by an external magnetic bias  $\mathbf{B}_0$ . In the absence of  $\mathbf{B}_0$ , InSb exhibits isotropic epsilon-near-zero (ENZ) and plasmonic behavior above and below its

plasma frequency, respectively, a frequency band which can be utilized for attaining invisibility using cloaks with permittivity less than that of free space. With realistic  $B_0$  magnitudes as high as 0.17 T, the gyroelectric properties of InSb enable the lift of mode degeneracy, and the induction of Zeeman-split type magnetoplasmonic modes that beat the fundamental single-channel limit. Moreover, we show that chains of such particles, where each one operates in its superscattering regime, enable giant *off-to-on* enhancement in scattering efficiency, as well as unprecedentedly-high forward scattering. These all-in-one designs allow for the implementation of functional and readily tunable optical devices.

## Keywords

Anisotropic semiconductor, magneto-optical, magnetoplasmonic, nondegenerate modes, superscattering, Zeeman-split.

Dynamically manipulating the scattering characteristics of resonant structures comprises a valuable platform for the development of functional, tunable optical devices enabling a variety of applications,<sup>1,2</sup> including optical sorting,<sup>3</sup> visible-to-invisible switching,<sup>4</sup> cloaking-to-scattering/superscattering switching<sup>5,6</sup>, directionality inversion,<sup>7-9</sup> all-optical switching,<sup>10</sup> multipolar interference,<sup>11</sup> quantum emitters,<sup>12</sup> or light-matter interaction enhancement at the subwavelength regime via superscattering operation.<sup>13</sup> A pathway to actively manipulating the scattering response is through external-agent based alteration of the material properties of the structure, which retains the geometry and operational wavelength fixed. Techniques to achieve this dynamic switching between different states include the electrically configurable liquid crystal based meta-optic devices which change the phase or the orientation of the surrounding liquid crystal,<sup>14</sup> the use of phase-change materials that allow for a permittivity change by transiting between amorphous and crystalline states using external laser beams,<sup>15</sup> magneto-optical media whose permittivity can be modified by an external magnetic bias,<sup>16</sup> ferromagnetic materials whose permeability can be manipulated via tem-

perature variations,<sup>17</sup> or ultrafast nonlinear optical switching based on light-induced change of a material’s dielectric permittivity (normally, to low values).<sup>18</sup>

In this work, we demonstrate that in optimized 3-D core-shell spherical particles consisting of a high-index dielectric core and an InSb semiconductor coating, we can exceed the fundamental single-channel limit of the scattering efficiency<sup>19</sup> by appropriately inducing a nondegenerate magnetoplasmonic resonance under an external magnetic field  $\mathbf{B}_0$ . In addition, while keeping the geometry and operational wavelength fixed, we can transform the configuration to an invisible state<sup>20</sup> simply by switching off this external  $\mathbf{B}_0$ . Furthermore, we demonstrate that chains of the considered particles enable, both, giant enhancement in the scattering efficiency and in the forward scattering direction as well—of key potential importance for a range of nanophotonic applications, including metalenses.<sup>21</sup> We also show that this *off-to-on* transition from invisibility to superscattering is robust under material losses and geometric deformations. The findings obtained from the presented formal semi-analytical solutions are in excellent agreement with full-wave finite element simulations (COMSOL<sup>22</sup>), establishing the validity of the proposed set-up.

We note that compared to previous two-dimensional (2-D)<sup>13,23</sup> or **3-D<sup>15,24,25</sup> superscattering schemes**, the underlying superscattering mechanism in our case is fundamentally different from the aforementioned implementations. In those works, superscattering becomes possible through an appropriately-engineered overlap between different TE and TM scattering channels, e.g., one corresponding to the core and the other to the coating<sup>15</sup>. Here, however, in the presence of an external magnetic field, TE/TM mode separation is no longer possible, and hybrid  $m$ - or Zeeman-split modes—where  $m$  is the spherical harmonics index—appear owing to the Faraday effect<sup>9,26,27</sup>. These superscattering modes are hybrid magnetoplasmonic modes of the InSb coating only, with mixed electric and magnetic character. This inherent mode-polarization mixing in  $m$ -split modes is the fundamental mechanism that here allows breaking the 3-D single-channel limit, and it therefore inherently differs from the overlap between modes of different origins reported in previous works<sup>13,15,23</sup>.

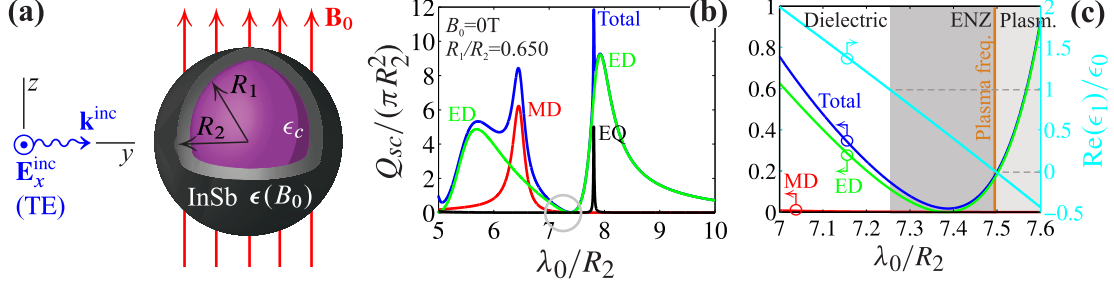


Figure 1: (a) Schematic representation of the proposed set-up. Linear TE polarized plane wave impinges at an angle of  $90^\circ$  with respect to the external magnetic field  $\mathbf{B}_0$ . (b) Spectrum in the subwavelength regime illustrating ENZ- and plasmonic-based transparency under null  $\mathbf{B}_0$  in the set-up of (a) with  $\epsilon_c = 20\epsilon_0$ ,  $R_2 = 20 \mu\text{m}$  and  $R_1/R_2 = 0.650$ . Blue: total normalized  $Q_{sc}$ ; red: MD term; green: ED term; black: EQ term. The gray circle indicates the region where transparency is achieved. (c) Zoom in the  $\lambda_0/R_2$  window indicated by the gray circle in (b). Blue/left axis: total normalized  $Q_{sc}$ ; red/left axis: MD term; green/left axis: ED term; cyan/right axis:  $\text{Re}(\epsilon_1)/\epsilon_0$  of the InSb coating above and below plasma frequency  $f_p = 2 \text{ THz}$  (shown by the vertical orange line at  $\lambda_0/R_2 = 7.495$ ). White region (dielectric):  $\text{Re}(\epsilon_1)/\epsilon_0 > 1$ ; dark-gray region (ENZ):  $0 < \text{Re}(\epsilon_1)/\epsilon_0 < 1$ ; bright-gray region (plasmonic):  $\text{Re}(\epsilon_1)/\epsilon_0 < 0$ .

**Proposed set-up and semi-analytical solution.** In Figure 1a we show the configuration of the forward-superscattering to invisibility magnetic switch. The main structure consists of a  $R_1$ -radius high permittivity  $\epsilon_c = 20\epsilon_0$  dielectric core—with  $\epsilon_0$  being the free space permittivity—coated by a  $R_2$ -radius shell consisting of semiconductor InSb. The whole configuration is located in free space, and can be exposed in external magnetic field  $\mathbf{B}_0 = B_0\mathbf{e}_z$ . Since  $\mathbf{B}_0$  is  $z$ -oriented, InSb permittivity tensor is expressed in cartesian coordinates by  $\epsilon(B_0) = \epsilon_1(B_0)(\mathbf{e}_x\mathbf{e}_x^T + \mathbf{e}_y\mathbf{e}_y^T) + i\epsilon_2(B_0)(\mathbf{e}_x\mathbf{e}_y^T - \mathbf{e}_y\mathbf{e}_x^T) + \epsilon_3\mathbf{e}_z\mathbf{e}_z^T$ —where  $T$  denotes transposition—with  $\epsilon_1(B_0) = \epsilon_0\epsilon_\infty\{1 - (\omega + iv)\omega_p^2/\omega/[(\omega + iv)^2 - \omega_c^2]\}$ ,  $\epsilon_2(B_0) = \epsilon_0\epsilon_\infty\{\omega_c\omega_p^2/\omega/[(\omega + iv)^2 - \omega_c^2]\}$  and  $\epsilon_3 = \epsilon_0\epsilon_\infty[1 - \omega_p^2/\omega/(\omega + iv)]$ .<sup>28</sup> In the aforementioned relations we use realistic material parameters where  $\epsilon_\infty = 15.6$  accounts for interband transitions,  $\omega_p = (N_e e^2/\epsilon_0/\epsilon_\infty/m^*)^{1/2} = 4\pi \times 10^{12} \text{ rad/s}$  is the plasma angular frequency (with  $N_e$  the electron density,  $e$  the elementary charge and  $m^* = 0.0142m_e$  electron's effective mass, where  $m_e$  is electron's rest mass),  $\omega_c = eB_0/m^*$  is cyclotron angular frequency, and  $v = 0.001\omega_p$  the damping angular frequency which accounts for losses. In case of null  $\mathbf{B}_0$ , InSb turns isotropic with  $\epsilon_1(0) \equiv \epsilon_3$  and  $\epsilon_2(0) = 0$ . For experimental implementation,

core-shell spheres in the micrometer size range, consisting of dielectric cores and semiconductor coatings, can be practically synthesized by shell growth condensation reaction methods<sup>29</sup>. In addition, the external magnetic field and the entire experimental procedure, can be routinely carried out using magnet-based set-ups<sup>30,31</sup>. In the present case, the spherical set-up is illuminated by a transverse electric (TE) plane wave—i.e., the incident electric field  $\mathbf{E}^{\text{inc}}$  is normal to the plane of incidence; therefore, if the plane of incidence is the  $yz$ -plane as shown in Figure 1a, then  $\mathbf{E}^{\text{inc}}$  is  $x$ -polarized—whose incident wavevector is normal to  $\mathbf{B}_0$ . To examine the electromagnetic (EM) response of the magnetic switch proposed in this work, the solution of EM plane wave scattering by dielectric-gyroelectric core-shell spheres is necessary. This is feasible by the discrete eigenfunction method employed in<sup>32,33</sup> for homogeneous spheres and spheroids. In Section I of the Supporting Information we extend that method and we rigorously develop a full-wave semi-analytical solution of EM scattering by core-shell dielectric-gyroelectric spheres, while, in Section II of the Supporting Information, we analyze its convergence. The scattering cross section is given by

$$Q_{sc} = \frac{\lambda_0^2}{\pi} \sum_{m=-n}^n \sum_{n=1}^{\infty} \left( |a_{mn}|^2 + |b_{mn}|^2 \right), \quad (1)$$

where  $\lambda_0$  is the free space wavelength,  $a_{mn}$ ,  $b_{mn}$  the expansion coefficients of the scattered electric field (see eq S2 of the Supporting Information), and  $m$ ,  $n$  the spherical harmonics and angular momentum indices, respectively. In the long wavelength limit, the spectrum is dominated by the electric dipolar (ED) and magnetic dipolar (MD) responses for which  $n = 1$ . In particular, for purely isotropic scatterers, the ED response is obtained when only the  $b_{1,1}$  expansion coefficient contributes in eq 1, while the MD response stems exclusively from  $a_{1,1}$ .

**Magnetically assisted superscattering and optimization.** When the MD response is negligible and the ED response dominates the spectrum, transparency can be achieved by utilizing an isotropic lossless ENZ coating with permittivity  $\epsilon_1 < \epsilon_0$  and a radii ratio

determined by<sup>34</sup>

$$\frac{R_1}{R_2} = \left[ \frac{(\epsilon_1 - \epsilon_0)(2\epsilon_1 + \epsilon_c)}{(\epsilon_1 - \epsilon_c)(2\epsilon_1 + \epsilon_0)} \right]^{1/3}. \quad (2)$$

By appropriately selecting  $\epsilon_1$ ,  $\epsilon_c$ , eq 2 yields the radii ratio for which cancellation of the ED term in the spectrum is achieved. eq 2 is ideally suited for lossless and non-dispersive materials. To make a rough estimation of a possible transparency window, using eq 2, we neglect losses by setting zero damping term  $v$  in Drude-Lorentz model of InSb, we set  $\epsilon_1 = 0.4929\epsilon_0$  as an average value of  $\epsilon_1$  in the range from 2 THz to 2.065 THz, and along with  $\epsilon_c = 20\epsilon_0$ , eq 2 yields  $R_1/R_2 = 0.650$ . This radii ratio can serve as a tentative basis also in our case, where the InSb coating is lossy and dispersive. **As it is shown below, by employing  $R_1/R_2 = 0.650$ , the total normalized  $Q_{sc}$  in the aforementioned spectral range stems almost solely from the ED contribution, while the MD response is negligible—see the following discussion below related to Figure 1c. Therefore the application of eq 2 is established since the ED response dominates this particular range of the spectrum.**

At first, we examine the optical response of the lossy and dispersive core-shell particle in the absence of  $\mathbf{B}_0$ , where InSb is isotropic. By employing the radii ratio  $R_1/R_2 = 0.650$ , we obtain the spectrum shown in Figure 1b. In blue line we show the total normalized  $Q_{sc}$  which involves all terms of eq 1; we keep  $N_c$  terms in the  $n$ -index series to ensure convergence (see Section II of the Supporting Information). In addition, we also depict the separate MD/ED and electric quadrupolar (EQ) terms. The latter one contributes to eq 1 by employing only the  $a_{1,2}$  expansion coefficient. The ED/MD resonances appearing in the range from  $\lambda_0/R_2 = 5$  up to  $\lambda_0/R_2 = 7$  in Figure 1b, are typical subwavelength resonances due to the high-index dielectric core. On the contrary, the EQ/ED peaks above  $\lambda_0/R_2 = 7.5$  are plasmonic resonances of the coating. This is because at frequencies below the plasma frequency  $f_p = \omega_p/(2\pi)$ , InSb changes its properties from ENZ to plasmonic. **To further discuss this behavior around the plasma frequency, in Figure 1c we illustrate the change of**

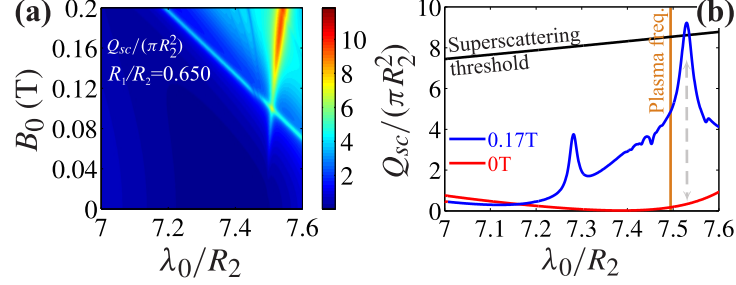


Figure 2: Application of external  $\mathbf{B}_0$ . The set-up is the same as in Figure 1. (a) Total normalized  $Q_{sc}$  vs  $B_0$  and  $\lambda_0/R_2$  in the transparency-enabled  $\lambda_0/R_2$  window as indicated by the gray circle in Figure 1b. (b) Comparison of total normalized  $Q_{sc}$  between null and non-null external  $\mathbf{B}_0$  states. Red:  $B_0 = 0$  T; blue:  $B_0 = 0.17$  T; black: superscattering threshold. The gray dashed arrowhead line depicts the precise  $\lambda_0/R_2 = 7.530$  of the *off-on* transition.

InSb's properties from ENZ to plasmonic, by focusing in the transition region indicated by the gray circle in Figure 1b. There, the two domains—ENZ/plasmonic—are marked by dark-gray and bright-gray colors, the boundary of which is determined by the plasma frequency at  $\lambda_0/R_2 = 7.495$  (or  $f_p = 2$  THz). The real part of the coating permittivity  $\text{Re}(\epsilon_1)$  depends almost linearly on the wavelength, as shown in Figure 1c. In particular,  $\text{Re}(\epsilon_1)/\epsilon_0 = 0$  at  $\lambda_0/R_2 = 7.495$ —which corresponds to frequency  $f_0$  equal to  $f_p$ —while  $\text{Re}(\epsilon_1)/\epsilon_0 \approx 1$  at  $\lambda_0/R_2 = 7.25$  ( $f_0 = 2.068$  THz). In brief, Figure 1(c) indicates that inside the ENZ region of the coating, the normalized  $Q_{sc}$ , which stems almost solely from the ED contribution—the MD contribution is negligible in this spectral window, as clearly depicted in Figure 1c—is suppressed, resulting in a respective transparency window.

In Figure 2a we show the map of the normalized  $Q_{sc}$ , versus the external  $B_0$  magnitude, in the wavelength window indicated by the gray circle in Figure 1b. All the other parameters of the configuration are the same with the ones used in Figure 1b. The deep blue region at  $B_0 = 0$  T in Figure 2a corresponds to the above mentioned transparency window where the normalized  $Q_{sc}$  is almost zero. By *switching on* the external magnetic field, and varying its magnitude, we can monitor the impact that it has on this transparency window. In particular, for  $B_0 \neq 0$  T, sharp peaks in intense red color appear, which correspond to high  $Q_{sc}/(\pi R_2^2)$  values. In Figure 2b we plot the normalized  $Q_{sc}$  for two particular choices of

$B_0$ , i.e.,  $B_0 = 0$  and  $B_0 = 0.17$  T. The first case ( $B_0 = 0$ ) is already discussed but shown for comparison. At  $B_0 = 0.17$  T, two dominant scattering Zeeman-split modes appear, where the longer-wavelength one has greater normalized  $Q_{sc}$  than the dipole-superscattering single-channel threshold, with the latter given by<sup>19</sup>

$$\frac{Q_{sc}}{\pi R_2^2} = \frac{3}{2\pi^2} \left( \frac{\lambda_0}{R_2} \right)^2. \quad (3)$$

The corresponding dipole-superscattering threshold is shown in Figure 2b in black. This mode breaks through the single-channel limit due to the mixed TE/TM character—see also the discussion of Figure 3 below and Section IV of the Supporting Information where a broader perspective of the Zeeman-split mechanism, involved in our configuration, is given. As shown in Figure 2b, the superscattering resonance at  $\lambda_0/R_2 = 7.530$  can be dramatically suppressed by *switching off* the external magnetic field, where the particle becomes almost transparent. This transition from superscattering operation— $Q_{sc}/(\pi R_2^2) = 9.223$  ( $B_0 = 0.17$  T) to almost transparency— $Q_{sc}/(\pi R_2^2) = 0.3339$  ( $B_0 = 0$  T), controlled entirely by the external magnetic bias, is pointed out with a dashed arrow in Figure 2b. We point out here that the lower-wavelength and smaller in amplitude Zeeman-split resonance in Figure 2b at  $\lambda_0/R_2 = 7.282$ , when  $B_0 = 0.17$  T, is much below the single-channel limit. Additionally, this mode does not exhibit unidirectional scattering, rendering it improper for the application studied here. Next, we define a figure of merit (FOM) as the ratio

$$\text{FOM} = \frac{\sigma_{B_0}}{\sigma_0}, \quad (4)$$

where  $\sigma_{B_0}$  is the bistatic scattering cross section  $\sigma(\theta, \varphi)$  in the forward direction—i.e.,  $\sigma_{B_0} \equiv \sigma(\theta = \pi/2, \varphi = \pi/2)$ —when the particle is at *on*-state/forward-superscattering with  $B_0 \neq 0$ , and  $\sigma_0$  is the bistatic scattering cross section, again in the forward direction, when the particle is at *off*-state/transparency with  $B_0 = 0$  T. For the specific example of Figure 2b we get  $\sigma_{B_0}/(\pi R_2^2) = 20.45$  and  $\sigma_0/(\pi R_2^2) = 0.4269$ , calculated precisely at  $\lambda_0/R_2 = 7.530$ . These

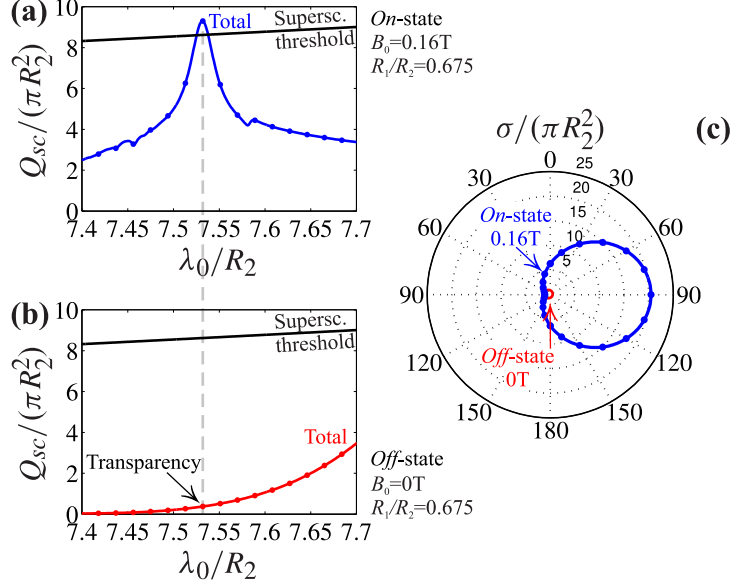


Figure 3: Engineering the magnetic switch for optimal operation at  $R_1/R_2 = 0.675$  and  $B_0 = 0.16$  T. The other values of parameters are the same as in Figure 1. (a) Spectrum in *on-state/superscattering* operation with  $B_0 = 0.16$  T. Blue: total normalized  $Q_{sc}$ /curve: our method/dots: COMSOL; black: superscattering threshold. (b) Spectrum in *off-state/transparency* operation with  $B_0 = 0$  T. Red: total normalized  $Q_{sc}$ /curve: our method/dots: COMSOL; black: superscattering threshold. The gray dashed vertical line depicts the value  $\lambda_0/R_2 = 7.532$  where the optimal *off-on* transition takes place. (c) Radiation pattern of normalized  $\sigma$  on  $yz$ -plane under  $\lambda_0/R_2 = 7.532$  excitation. Blue: *on-state/forward* superscattering when  $B_0 = 0.16$  T/curve: our method/dots: COMSOL; red: *off-state/transparency* when  $B_0 = 0$  T.

values yield a FOM = 47.90. In Section III of the Supporting Information we show that for a given  $B_0 \neq 0$ , there exists an optimal  $R_1/R_2$  ratio for which FOM is maximized, yet the superscattering state is maintained. The FOM for Figure 2b for the selected  $B_0 = 0.17$  T is not the maximum one; the maximal value, as computed in the Supporting Information, is achieved at the optimized ratio  $R_1/R_2 = 0.625$ .

**Invisibility to superscattering magnetic switch.** In what follows we demonstrate the realization of the invisibility to superscattering magnetic switch for one of the optimized states presented in Section III of the Supporting Information. We pick up the optimized structure with  $R_1/R_2 = 0.675$  at  $B_0 = 0.16$  T. We clarify here that any state can be used to demonstrate the magnetic switch. In particular, the selected  $R_1/R_2 = 0.675$  ( $B_0 = 0.16$  T) scheme has lower FOM as compared to the  $R_1/R_2 = 0.715$  ( $B_0 = 0.14$  T) scheme, but the

latter has greater value in the total normalized  $Q_{sc}$  at *off*-state, thus constituting it less transparent as compared to the former scheme. Figure 3a depicts the total normalized  $Q_{sc}$  for the *on*-state operation. We note in passing that, for an isotropic spherical particle, the  $m$ -mode index in eq 1 is degenerate, which means that a multipolar mode of electric or magnetic type is only characterized by the angular momentum index  $n$ . However, this is not the case for gyroelectric spherical particles, as in the present case, where the lifting of the  $m$ -degeneracy leads to  $2n + 1$  separate Zeeman-split modes<sup>26,27</sup> for each *parent* mode. The coupling of each one of such modes with the external radiation strongly depends on the angle of incidence and polarization.<sup>26,35</sup> In Section V of the Supporting Information we study the effect of incidence angle and polarization on such modes. Our full-wave semi-analytical calculations show that, for TE-polarized light incident normal to the magnetization axis—see Figure 1a—the high peak at  $\lambda_0/R_2 = 7.532$  shown in Figure 3a, beats the superscattering limit. The physical mechanism behind this scattering maximization is attributed to the polarization mixing—TE-TM hybridization—caused by Faraday effect due to the strong interaction between the impinging  $\mathbf{E}^{\text{inc}}$  and the magnetization occurring by the external  $\mathbf{B}_0$ . This Zeeman-split mode observed at  $\lambda_0/R_2 = 7.532$  is understood as one of the magnetoplasmon polaritons excited in the magnetized InSb coating<sup>36–38</sup>—see also Section IV of the Supporting Information. Obviously, this is not the case when InSb is not magnetized, as in the case of Figure 1b where the coating exhibits purely plasmonic properties and the spectrum is dominated by  $m$ -degenerate ED and EQ resonances only. The respective spectrum at *off*-state is shown in Figure 3b, using the same scale as the one in Figure 3a. At  $\lambda_0/R_2 = 7.532$ , the system is almost transparent with normalized  $Q_{sc}$  being significantly suppressed at  $Q_{sc}/(\pi R_2^2) = 0.3746$ . With a  $Q_{sc}/(\pi R_2^2) = 9.302$  when  $B_0 = 0.16$  T, this *off*-to-*on* transition results in a 2383% enhancement in  $Q_{sc}$ . Figure 3c depicts the radiation pattern when the system operates at  $\lambda_0/R_2 = 7.532$ . The forward-superscattering operation is achieved with a FOM = 50.38 and an almost null radiation pattern when  $B_0 = 0$  T. To validate our findings, we fully compare our semi-analytical solution with

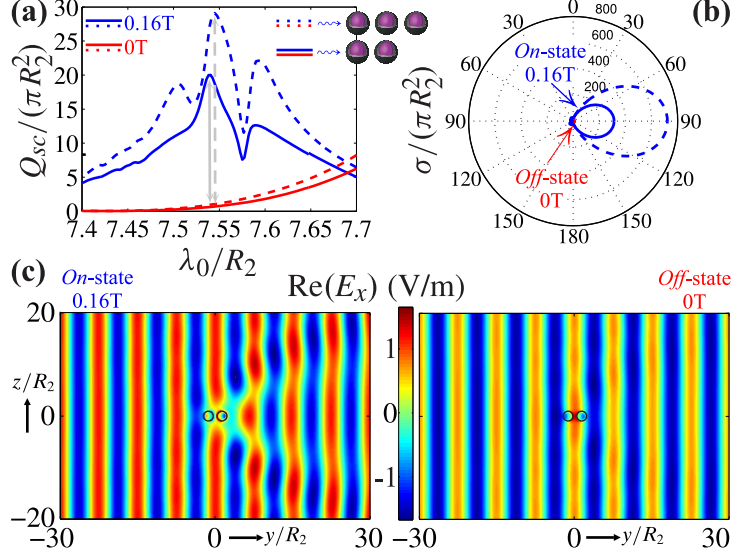


Figure 4: Engineering a dimer and trimer for enhanced FOM using COMSOL. The gap between the spheres is  $10 \mu\text{m}$  while the remaining values of parameters are the same as in Figure 3. (a) Spectrum at *on/off*-state with  $B_0 = 0.16 \text{ T}/B_0 = 0 \text{ T}$ . Blue: total normalized  $Q_{sc}$  at *on*-state/solid: dimer/dashed: trimer; red: total normalized  $Q_{sc}$  at *off*-state/solid: dimer/dashed: trimer. (b) Radiation pattern of normalized  $\sigma$  on  $yz$ -plane under  $\lambda_0/R_2 = 7.541$  excitation. Blue: *on*-state/forward scattering when  $B_0 = 0.16 \text{ T}$ /solid: dimer/dashed: trimer; red: *off*-state/transparency when  $B_0 = 0 \text{ T}$ /solid: dimer/dashed: trimer (the two latter red curves are negligible as compared to the *on*-state curves). (c) Dimer near-field of  $\text{Re}(E_x)$  on  $yz$ -plane under *on*-state (left) and *off*-state (right) activity.

COMSOL's finite-element solver. The total normalized  $Q_{sc}$ , as obtained by our method, is in full agreement with COMSOL, with the latter being depicted by the blue and red dots in Figures 3a–c. To have a degree of comparison, our method yields  $Q_{sc}/(\pi R_2^2) = 9.302$  and  $0.3746$  at the magnetoplasmonic resonance and at the transparency state, respectively, when  $\lambda_0/R_2 = 7.532$ . COMSOL's respective values are  $Q_{sc}/(\pi R_2^2) = 8.892$  and  $0.3746$ , while the superscattering threshold is  $8.622$ . In addition, the radiation pattern depicted in Figure 3c is in full agreement with COMSOL. These results are robust under variations of the problem parameters, such as the geometrical shape and the loss in InSb permittivity. In Section VI of the Supporting Information we demonstrate the robustness of the magnetic switch due to (i) shape perturbation, by considering shapes that deviate from the sphere, and (ii) loss variation, by varying InSb's damping angular frequency.

Next, in Figure 4 we apply the principles presented in Figure 3 to a chain-like config-

uration of such particles, showing that this leads to a giant increase in the FOM and in the *off*-to-*on* enhancement in  $Q_{sc}$ . In particular, Figure 4a presents the total normalized  $Q_{sc}$  of a dimer and trimer of core-shell spheres, for the incident wave of Figure 1a. At  $\lambda_0/R_2 = 7.541$ , the dimer is almost transparent with  $Q_{sc}/(\pi R_2^2) = 0.6331$  when  $B_0 = 0$  T. With a  $Q_{sc}/(\pi R_2^2) = 20.03$  when  $B_0 = 0.16$  T, this *off*-to-*on* transition results in a giant 3064% enhancement in  $Q_{sc}$ . We note that the respective values for trimer are red-shifted, located at  $\lambda_0/R_2 = 7.545$  with  $Q_{sc}/(\pi R_2^2) = 29.09$  at  $B_0 = 0.16$  T and  $Q_{sc}/(\pi R_2^2) = 0.9631$  at  $B_0 = 0$  T. These yield a 2920% enhancement in  $Q_{sc}$ , at the same high level as with the dimer. Furthermore, the radiation pattern in Figure 4b reveals that this configuration allows for a further increased FOM = 78.2 for the dimer, or 61.7 for the trimer, as compared to the single sphere case—in all cases, by keeping the same magnetic bias at 0.16 T. Figure 4c illustrates the  $\text{Re}(E_x)$  on  $yz$ -plane for *on*- and *off*-state dimer activity. Figure 4c/right confirms the invisibility state since the incoming wave passes through the scatterer almost unperturbed, while Figure 4c/left clearly illustrates the forward-scattering propagation along the positive  $y$ -axis. This dramatic increase in the scattering efficiency of the magnetized chain-like configuration indicates a cascade effect, where essentially a scattering amplification is transferred from each particle to the next one. We note here that the dimer and trimer configurations demonstrated in Figure 4 are not geometrically optimized to achieve maximum or ideal performance. Overall, similar, appropriately optimized, oligomers could serve as building blocks for applications such as magnetically-tunable metasurfaces and metalenses.

**Conclusion.** Based on a rigorous semi-analytical solution of the 3-D EM scattering problem from dielectric-gyroelectric spheres, corroborated by full-wave simulations, we presented a high-permittivity/semiconductor structure capable of breaking the fundamental single-channel limit of the scattering efficiency. This operation is established by inducing, in the subwavelength regime, nondegenerate magnetoplasmonic modes when applying a low external magnetic bias in the range 0.14 T–0.17 T. For the same operational wavelength and core-shell radii, for which superscattering operation was observed, we also showed how

3-D invisibility can be attained, solely by turning off the external magnetic field. We also reported that chains of such particles, each operating in its superscattering regime, can enormously enhance the scattering efficiency, as well as the forward scattering. Our findings could pave the way towards the design of functional and readily tunable optical devices, including state-of-the-art optical metasurfaces and metalenses.<sup>21</sup>

## Acknowledgement

G.P.Z., E.A., and K.L.T. were supported by the General Secretariat for Research and Technology (GSRT) and the Hellenic Foundation for Research and Innovation (HFRI) under Grant No. 1819.

## Supporting Information Available

Development of the solution, analysis of its convergence, optimization, discussion of Zeeman-split magnetoplasmons, effect of incidence angle and polarization on mode excitation, and robustness of the magnetic switch due to geometry and loss variation.

## References

- (1) Kuznetsov, A. I.; Miroshnichenko, A. E.; Brongersma, M. L.; Kivshar, Y. S.; Luk'yanchuk, B. Optically resonant dielectric nanostructures. *Science* **2016**, *354*, aag2472.
- (2) Tsakmakidis, K. L.; Hess, O.; Boyd, R. W.; Zhang, X. Ultraslow waves on the nanoscale. *Science* **2017**, *358*, eaan5196.
- (3) Shilkin, D. A.; Lyubin, E. V.; Shcherbakov, M. R.; Lapine, M.; Fedyanin, A. A. Directional optical sorting of silicon nanoparticles. *ACS Photonics* **2017**, *4*, 2312–2319.

- (4) Rybin, M. V.; Samusev, K. B.; Kapitanova, P. V.; Filonov, D. S.; Belov, P. A.; Kivshar, Y. S.; Limonov, M. F. Switchable invisibility of dielectric resonators. *Phys. Rev. B* **2017**, *95*, 165119.
- (5) Kort-Kamp, W. J. M.; Rosa, F. S. S.; Pinheiro, F. A.; Farina, C. Molding the flow of light with a magnetic field: plasmonic cloaking and directional scattering. *J. Opt. Soc. Am. A* **2014**, *31*, 1969–1976.
- (6) Huang, Y.; Shen, Y.; Min, C.; Veronis, G. Switching photonic nanostructures between cloaking and superscattering regimes using phase-change materials [Invited]. *Opt. Mat. Expr.* **2018**, *8*, 1672–1685.
- (7) Arruda, T. J.; Martinez, A. S.; Pinheiro, F. A. Electromagnetic energy and negative asymmetry parameters in coated magneto-optical cylinders: Applications to tunable light transport in disordered systems. *Phys. Rev. A* **2016**, *94*, 033825.
- (8) Liu, M. Q.; Zhao, C. Y.; Wang, B. X. Active tuning of directional scattering by combining magneto-optical effects and multipolar interferences. *Nanoscale* **2018**, *10*, 18282–18290.
- (9) Zouros, G. P.; Kolezas, G. D.; Almpanis, E.; Baskourellos, K.; Stefański, T.; Tsakmakidis, K. L. Magnetic switching of Kerker scattering in spherical microresonators. *Nanophotonics* **2020**, *9*, 4033–4041.
- (10) Shcherbakov, M. R.; Vabishchevich, P. P.; Shorokhov, A. S.; Chong, K. E.; Choi, D.-Y.; Staude, I.; Miroshnichenko, A. E.; Neshev, D. N.; Fedyanin, A. A.; Kivshar, Y. S. Ultrafast All-Optical Switching with Magnetic Resonances in Nonlinear Dielectric Nanostructures. *Nano Lett.* **2015**, *15*, 6985–6990.
- (11) Limonov, M. F.; Rybin, M. V.; Poddubny, A. N.; Kivshar, Y. S. Fano resonances in photonics. *Nature Photon.* **2017**, *11*, 543–554.

- (12) Cihan, A. F.; Curto, A. G.; Raza, S.; Kik, P. G.; Brongersma, M. L. Silicon Mie resonators for highly directional light emission from monolayer MoS<sub>2</sub>. *Nature Photon.* **2018**, *12*, 284–290.
- (13) Qian, C.; Lin, X.; Yang, Y.; Xiong, X.; Wang, H.; Li, E.; Kaminer, I.; Zhang, B.; Chen, H. Experimental Observation of Superscattering. *Phys. Rev. Lett.* **2019**, *122*, 063901.
- (14) Komar, A.; Fang, Z.; Bohn, J.; Sautter, J.; Decker, M.; Miroshnichenko, A.; Pertsch, T.; Brener, I.; Kivshar, Y. S.; Staude, I.; Neshev, D. N. Electrically tunable all-dielectric optical metasurfaces based on liquid crystals. *Appl. Phys. Lett.* **2017**, *110*, 071109.
- (15) Lepeshov, S.; Krasnok, A.; Alù, A. Nonscattering-to-Superscattering Switch with Phase-Change Materials. *ACS Photonics* **2019**, *6*, 2126–2132.
- (16) Kort-Kamp, W. J. M.; Rosa, F. S. S.; Pinheiro, F. A.; Farina, C. Tuning Plasmonic Cloaks with an External Magnetic Field. *Phys. Rev. Lett.* **2013**, *111*, 215504.
- (17) Arruda, T. J.; Martinez, A. S.; Pinheiro, F. A. Tunable multiple Fano resonances in magnetic single-layered core-shell particles. *Phys. Rev. A* **2015**, *92*, 023835.
- (18) Caspani, L.; Kaipurath, R. P. M.; Clerici, M.; Ferrera, M.; Roger, T.; Kim, J.; Kinsey, N.; Pietrzyk, M.; Falco, A. D.; Shalaev, V. M.; Boltasseva, A.; Faccio, D. Enhanced Nonlinear Refractive Index in  $\epsilon$ -Near-Zero Materials. *Phys. Rev. Lett.* **2016**, *116*, 233901.
- (19) Tribelsky, M. I.; Luk'yanchuk, B. S. Anomalous Light Scattering by Small Particles. *Phys. Rev. Lett.* **2006**, *97*, 263902.
- (20) Tsakmakidis, K. L.; Reshef, O.; Almpanis, E.; Zouros, G. P.; Mohammadi, E.; Saadat, D.; Sohrabi, F.; Fahimi-Kashani, N.; Etezad, D.; Boyd, R. W.; Altug, H. Ultra-broadband 3D invisibility with fast-light cloaks. *Nat. Commun.* **2019**, *10*, 4859.

- (21) Neshev, D.; Aharonovich, I. Optical metasurfaces: new generation building blocks for multi-functional optics. *Light Sci. Appl.* **2018**, *7*, 1–5.
- (22) COMSOL Multiphysics® v. 5.1. www.comsol.com. COMSOL AB, Stockholm, Sweden.
- (23) Ruan, Z.; Fan, S. Superscattering of Light from Subwavelength Nanostructures. *Phys. Rev. Lett.* **2010**, *105*, 013901.
- (24) Ruan, Z.; Fan, S. Design of subwavelength superscattering nanospheres. *Appl. Phys. Lett.* **2011**, *98*, 043101.
- (25) Liu, W. Ultra-directional super-scattering of homogenous spherical particles with radial anisotropy. *Opt. Expr.* **2015**, *23*, 14734–14743.
- (26) Almpanis, E. Dielectric magnetic microparticles as photomagnonic cavities: Enhancing the modulation of near-infrared light by spin waves. *Phys. Rev. B* **2018**, *97*, 184406.
- (27) Almpanis, E.; Zouros, G. P.; Pantazopoulos, P. A.; Tsakmakidis, K. L.; Papanikolaou, N.; Stefanou, N. Spherical optomagnonic microresonators: Triple-resonant photon transitions between Zeeman-split Mie modes. *Phys. Rev. B* **2020**, *101*, 054412.
- (28) Tsakmakidis, K. L.; Shen, L.; Schulz, S. A.; Zheng, X.; Upham, J.; Deng, X.; Altug, H.; Vakakis, A. F.; Boyd, R. W. Breaking Lorentz reciprocity to overcome the time-bandwidth limit in physics and engineering. *Science* **2017**, *356*, 1260–1264.
- (29) Lechner, A. M.; Feller, T.; Song, Q.; Kopera, B. A. F.; Heindl, L.; Drechsler, M.; Rosenfeldt, S.; Retsch, M. Scalable synthesis of smooth PSTiO<sub>2</sub> core-shell and TiO<sub>2</sub> hollow spheres in the (sub) micron size range: understanding synthesis and calcination parameters. *Colloid Polym. Sci.* **2020**, *298*, 867–878.
- (30) Weiss, C.; Wallenstein, R.; Beigang, R. Magnetic-field-enhanced generation of terahertz radiation in semiconductor surfaces. *Appl. Phys. Lett.* **2000**, *77*, 4160.

- (31) Haigh, J. A.; Langenfeld, S.; Lambert, N. J.; Baumberg, J. J.; Ramsay, A. J.; Nunnenkamp, A.; Ferguson, A. J. Magneto-optical coupling in whispering-gallery-mode resonators. *Phys. Rev. A* **2015**, *92*, 063845.
- (32) Li, J. L.-W.; Ong, W.-L. A new solution for characterizing electromagnetic scattering by a gyroelectric sphere. *IEEE Trans. Antennas Propag.* **2011**, *59*, 3370–3378.
- (33) Kolezas, G. D.; Zouros, G. P.; Tsakmakidis, K. L. Engineering Subwavelength Nanoantennas in the Visible by Employing Resonant Anisotropic Nanospheroids. *IEEE J. Sel. Top. Quantum Electron.* **May/June 2019**, *25*, 4700912.
- (34) Alù, A.; Engheta, N. Achieving transparency with plasmonic and metamaterial coatings. *Phys. Rev. E* **2005**, *72*, 016623.
- (35) Varytis, P.; Stefanou, N. Plasmon-driven large Hall photon currents in light scattering by a core-shell magnetoplasmonic nanosphere. *J. Opt. Soc. Am. B* **2016**, *33*, 1286–1290.
- (36) Brionand, J. J.; Wallis, R. F.; Hartstein, A.; Burstein, E. Theory of Surface Magnetoplasmons in Semiconductors. *Phys. Rev. Lett.* **1972**, *28*, 1455–1458.
- (37) Chen, S.; Fan, F.; He, X.; Chen, M.; Chang, S. Multifunctional magneto-metasurface for terahertz one-way transmission and magnetic field sensing. *Applied optics* **2015**, *54*, 9177–9182.
- (38) Xia, L.; Zhang, X.; Wang, D.; Zhang, W.; Han, J. Terahertz surface magnetoplasmons modulation with magnetized InSb hole array sheet. *Opt. Commun.* **2019**, *446*, 84–87.